MULTIFREQUENCY PHOTO-POLARIMETRIC WEBT OBSERVATION CAMPAIGN ON THE BLAZAR S5 0716 +714: SOURCE MICROVARIABILITY AND SEARCH FOR CHARACTERISTIC TIMESCALES[*]

G. Bhatta[1], Ł. Stawarz[1], M. Ostrowski[1], A. Markowitz[2], H. Akitaya[3], A. A. Arkharov[4], R. Bachev[5], E. Benítez[6], G. A. Borman[7], D. Carosati[8,9], A. D. Cason[10], R. Chanishvili[11], G. Damljanovic[12], S. Dhalla[13], A. Frasca[14], D. Hiriart[15], S-M. Hu[16], R. Itoh[17], D. Jableka[1], S. Jorstad[18,19], M. D. Jovanovic[12], K. S. Kawabata[3], S. A. Klimanov[4], O. Kurtanidze[11,20,21], V. M. Larionov[4,19], D. Laurence[13], G. Leto[14], A. P. Marscher[18], J. W. Moody[22], Y. Moritani[23], J. M. Ohlert[24], A. Di Paola[25], C. M. Raiteri[26], N. Rizzi[27], A. C. Sadun[28], M. Sasada[18], S. Sergeev[7], A. Strigachev[5], K. Takaki[17], I. S. Troitsky[19], T. Ui[17], M. Villata[26], O. Vince[12], J. R. Webb[13], M. Yoshida[3], AND S. Zola[1,29]

[1] Astronomical Observatory of Jagiellonian University, ul. Orla 171, 30-244 Krakow, Poland; gopalbhatta716@gmail.com
[2] Center for Astrophysics and Space Sciences, University of California, San Diego, 9500 Gilman Dr., La Jolla, CA 92093-0424, USA
[3] Hiroshima Astrophysical Science Center, Hiroshima University, Higashi-Hiroshima, Hiroshima 739-8526, Japan
[4] Main (Pulkovo) Observatory of RAS, Pulkovskoye shosse, 60, 196140 St. Petersburg, Russia
[5] Institute of Astronomy, Bulgarian Academy of Sciences, 72, Tsarigradsko Shosse Blvd., 1784 Sofia, Bulgaria
[6] Instituto de Astronomía, Universidad Nacional Autónoma de México, Mexico DF, Mexico
[7] Crimean Astrophysical Observatory, P/O Nauchny, Crimea, 298409, Russia
[8] EPT Observatories, Tijarafe, La Palma, Spain
[9] INAF, TNG Fundacion Galileo Galilei, La Palma, Spain
[10] Private address, 105 Glen Pine Trail, Dawnsonville, GA 30534, USA
[11] Abastumani Observatory, Mt. Kanobili, 0301 Abastumani, Georgia
[12] Astronomical Observatory, Volgina 7, 11060 Belgrade, Serbia
[13] Florida International University, Miami, FL 33199, USA
[14] INAF—Osservatorio Astrofisico di Catania, Italy
[15] Instituto de Astronomía, Universidad Nacional Autónoma de México, Ensenada, Mexico
[16] Shandong Provincial Key Laboratory of Optical Astronomy and Solar-Terrestrial Environment, Institute of Space Sciences, Shandong University at Weihai, 264209 Weihai, China
[17] Department of Physical Science, Hiroshima University, Higashi-Hiroshima, Hiroshima 739-8526, Japan
[18] Institute for Astrophysical Research, Boston University, 725 Commonwealth Ave., Boston, MA 02215, USA
[19] Astronomical Institute, St. Petersburg State University, Universitetskij Pr. 28, Petrodvorets, 198504 St. Petersburg, Russia
[20] Engelhardt Astronomical Observatory, Kazan Federal University, Tatarstan, Russia
[21] Landessternwarte Heidelberg-Konigstuhl, Germany
[22] Physics and Astronomy Department, Brigham Young University, N283 ESC, Provo, UT, 84602, USA
[23] Kavli Institute for the Physics and Mathematics of the universe (KavliI PMU), The University of Tokyo, 5-1-5 Kashiwa-no-Ha, Kashiwa City Chiba, 277-8583, Japan
[24] Astronomie Stiftung Tebur, Fichtenstrasse 7, D-65468 Trebur, Germany
[25] INAF—Osservatorio Astronomico di Roma, via Frascati 33, I-00040 Monte Porzio, Italy
[26] INAF—Osservatorio Astrofisico di Torino, Italy
[27] Sirio Astronomical Observatory Castellana Grotte, Italy
[28] Department of Physics, Univ. of Colorado Denver, CO, USA
[29] Mt. Suhora Observatory, Pedagogical University, ul. Podchorazych 2, 30-084 Krakow, Poland

ABSTRACT

Here we report on the results of the Whole Earth Blazar Telescope photo-polarimetric campaign targeting the blazar S5 0716+71, organized in 2014 March to monitor the source simultaneously in *BVRI* and near-IR filters. The campaign resulted in an unprecedented data set spanning ~110 hr of nearly continuous, multiband observations, including two sets of densely sampled polarimetric data mainly in the *R* filter. During the campaign, the source displayed pronounced variability with peak-to-peak variations of about 30% and "bluer-when-brighter" spectral evolution, consisting of a day-timescale modulation with superimposed hour-long microflares characterized by ~0.1 mag flux changes. We performed an in-depth search for quasi-periodicities in the source light curve; hints for the presence of oscillations on timescales of ~3 and ~5 hr do not represent highly significant departures from a pure red-noise power spectrum. We observed that, at a certain configuration of the optical polarization angle (PA) relative to the PA of the innermost radio jet in the source, changes in the polarization degree (PD) led the total flux variability by about 2 hr; meanwhile, when the relative configuration of the polarization and jet angles altered, no such lag could be noted. The microflaring events, when analyzed as separate pulse emission components, were found to be characterized by a very high PD (>30%) and PAs that differed substantially from the PA of the underlying background component, or from the radio jet positional angle. We discuss the results in the general context of blazar emission and energy dissipation models.

Key words: acceleration of particles – BL Lacertae objects: individual (S5 0716+714) – galaxies: active – galaxies: jets – polarization – radiation mechanisms: non-thermal

1. INTRODUCTION

Blazars, a subclass of radio-loud active galactic nuclei (AGNs), are usually identified by their Doppler-boosted nonthermal emission across the entire electromagnetic spectrum, originating from relativistic jets aligned near the line of sight (e.g., Meier 2012). They exhibit significant, often dramatic variability at different wavelengths and on diverse timescales, ranging from minutes up to years and decades. In particular, flux fluctuations by a few percent observed on timescales of minutes and hours are usually termed as an intraday/intranight variability (IDV/INV), or a microvariability (Wagner & Witzel 1995). Blazar microvariability at various frequencies has been studied by a number of authors since the late 1970s and was initially thought to result from the instrumental artifacts or external causes (environmental scintillation, gravitational microlensing, etc.; see, e.g., Schneider & Weiss 1987; Melrose 1994). Later, however, with the improvement of sensitive instruments such as charged coupled device (CCD) cameras and polarimetric measurements, those rapid and small-amplitude brightness fluctuations were fairly proved to be source intrinsic, and in addition to originate in the innermost parts of relativistic jets (e.g., Pollock et al. 2007; Sasada et al. 2008; Goyal et al. 2012). Since the blazar optical emission zone is not spatially resolved on (sub)-milliarcsecond scales by any currently operating telescopes, the study of microvariabilty can be therefore used to understand the structure of AGN outflows close to/at the jet base, and to constrain the main physical processes operating therein that shape the production of high-energy particles and nonthermal emission of blazar sources. Yet, despite a substantial observational effort, as well as a comprehensive theoretical discussion on the topic, with various models and scenarios proposed, blazar variability (and microvariability in particular) is still relatively poorly understood.

The polarimetric blazar variability in the optical band has been subjected to an extensive investigation in the past. The temporal polarization changes, observed on timescales from minutes to years, in most of the cases appear random, with no obvious or only a weak correlation between the polarization degree (PD) and the total flux (e.g., Hagen-Thorn 1980; Moore et al. 1982; Tommasi et al. 2001; Cellone et al. 2007; Ikejiri et al. 2011; Itoh et al. 2013; Raiteri et al. 2013; Gaur et al. 2014). Only in some particular sources during certain periods have the polarized and total fluxes been shown to vary in accord (e.g., Tosti et al. 1998; Hagen-Thorn et al. 2008; Agudo et al. 2011; Sorcia et al. 2013; Bhatta et al. 2015). Also, more recently, several cases of prominent swings/rotations in the optical polarization angle (PA) accompanying high-energy γ-ray outbursts of the brightest blazars have been reported (Marscher et al. 2008, 2010; Abdo et al. 2010; Jorstad et al. 2010; Larionov et al. 2013; Blinov et al. 2015). These results imply altogether a complex magnetic field structure that determines the observed properties of the blazar synchrotron emission at optical wavelengths, including both the large-scale uniform component (often modeled in terms of a "grand-design" helix) and a smaller-scale turbulent component (eventually only partly organized by the passage of shock waves and/or velocity shear within the outflow).

S5 0716+714 is one of the best known BL Lac objects, at a redshift of approximately $z = 0.31 \pm 0.08$ (see Nilsson et al. 2008; Danforth et al. 2013), classified as an "intermediate-synchrotron-peaked" blazar based on the location of its synchrotron peak in the $\nu F_\nu - \nu$ representation around frequencies of $\sim 10^{14}-10^{15}$ Hz (Ackermann et al. 2011). Since its discovery in 1979 by Kuhr et al. (1981), it has been the subject of numerous studies across the entire available electromagnetic spectrum, due to its brightness, its high declination in the sky, and its never-ceasing variability with almost 100% duty cycle (e.g., Heidt & Wagner 1996). At radio frequencies, S5 0716+714 appears on milliarcsecond scales as a flat-spectrum, IDV, and superluminal source, characterized by apparent velocities of various jet features reaching $37c$ (Jorstad et al. 2001; Bach et al. 2005; Rani et al. 2015) and a very high brightness temperature of the compact core (Ostorero et al. 2006). The X-ray emission continuum of the blazar is, in general, concave, marking the transition from the synchrotron to the inverse-Compton emission components in the observed spectrum (Ferrero et al. 2006; Foschini et al. 2006). S5 0716 +714 has been also detected at γ-ray photon energies by EGRET, *AGILE*, and *Fermi*-LAT (see, e.g., Ghisellini et al. 1997; Villata et al. 2008; Rani et al. 2013; Liao et al. 2014, and references therein), as well as by the MAGIC Cerenkov telescope (Anderhub et al. 2009).

At optical frequencies, S5 0716+714 appears as a bright, highly polarized, and highly variable source. Long-term optical light curves of the blazar are presented in Nesci et al. (2005) and Raiteri et al. (2003), and its general optical polarization properties are discussed in Impey et al. (2000) and Ikejiri et al. (2011). It was shown repeatedly that optical flux changes of S5 0716+714 do not correlate with radio variability (Raiteri et al. 2003; Ostorero et al. 2006), but instead with γ-ray flares (e.g., Villata et al. 2008; Rani et al. 2013; Liao et al. 2014), flares that in addition seem to be accompanied by large swings in the optical PA (Larionov et al. 2013; Chandra et al. 2015). Quasi-periodicity has been claimed in the optical light curves of the source for different epochs and at various timescales of hours, days, and years (Raiteri et al. 2003; Gupta et al. 2008, 2009, 2012). The optical microvariability of S5 0716+714 has been widely investigated by a number of authors, who found high or very high INV duty cycles, often (though not always) bluer-when-brighter spectral behavior, red-noise-type power spectra, and in some cases clear PD–flux correlations (Nesci et al. 2002; Montagni 2006; Sasada et al. 2008; Poon et al. 2009; Stalin et al. 2009; Carini et al. 2011; Chandra et al. 2011; Wu et al. 2012; Zhang et al. 2012; Dai et al. 2013; Hu et al. 2014; Bhatta et al. 2015; Agarwal et al. 2016).

Here we present the result of the multifrequency photometric and polarimetric monitoring campaign on S5 0716+714 through the Whole Earth Blazar Telescope (WEBT), which took place from 2014 March 2 to 6 (see Section 2). The main objective of the campaign was to monitor the source continuously for an extended period of time, to study its variations in flux, color, PD, and PA simultaneously and with unprecedented details, building on the previously undertaken successful WEBT monitoring campaigns targeting the blazar (by Villata et al. 2000 in 1999 February 16–19, Ostorero et al. 2006 in 2003 November 6–20, and Bhatta et al. 2013 in 2009 February 22–25). With the given duration of the campaign and its extremely dense, minute-scale sampling of the source light curve, the data could be subjected to a meaningful and robust time-series analysis, in search of temporal characteristics (including possible periodicity) on timescales from a few hours to a day (Section 3), i.e., the timescales that are basically unconstrained in either intranight

Table 1
Observatories Contributing to the 2014 WEBT Campaign on S5 0716+714

No.	Observatory	Telescope	Filter (PH)	Filter (PL)
1	Abastumani Obs., Georgia	70 cm	BVRI	⋯
2	Astronomical Obs., Kraków, Poland	50 cm	BVRI	⋯
3	Astronomical Station Vidojevica, Serbia	60 cm	BVRI	⋯
4	Belogradchik, Bulgaria	60 cm	BVRI	⋯
5	Crimean Astrophysical Obs., Russia	70 cm	BVRI	R
6	Campo Imperatore, Italy	110 cm	JHK	⋯
7	EPT Observatories Tijarafe La Palma Spain	40 cm Ritchey Chretien	R	⋯
8	Fairborn, Arizona, USA	APT 80 cm	BVRI	⋯
9	Higashi-Hiroshima, Kanata, Japan	150 cm	BVRI	R
10	L'Ampolla, Spain	36 cm	BVRI	⋯
11	Lowell Obs., Perkins, Flagstaff, AZ, USA	180 cm	BVRI	BVRI
12	Michael Adrian Obs., Germany	120 cm	BVRI	⋯
13	Astronomical Obs. Sirio Castellana Grotte, Italy	25 cm	R	⋯
14	SARA/Kitt Peak, USA	90 cm	BVRI	⋯
15	St. Petersburg University, Russia	40 cm	BVRI	WL
16	Suhora Observatory, Poland	90 cm	BVRI	⋯
17	T-11 Mayhill, New Mexico, USA	51 cm	BVRI	⋯
18	T-21 Mayhill, New Mexico, USA	43 cm	BVRI	⋯
19	T-24 Auberry, California, USA	61 cm	VI	⋯
20	Weihai Obs. of Shandong Univ., China	100 cm	BVRI	

Note. PH → photometric; PL → polarimetric; WL → white light.

observations conducted by a single ground-based telescope or typical long-term monitoring programs consisting of individual exposures isolated by days and weeks. The gathered rich data set constrains uniquely the physics of the emission zone in S5 0716+714, and blazar emission models in general (Section 4).

2. OBSERVATIONS

The WEBT[30] multifrequency photometric and polarimetric monitoring campaign on S5 0716+714 was originally scheduled for 2014 March 3 and 4, but due to an extraordinary participation of the observers all around the globe, it had been extended to 5 days. All in all, 26 observers from 20 observatories monitored the source in various photo-polarimetric filters from 2014 March 2 to 6. During the campaign, the weather, on most of the telescope sites, was photometric enough to allow for a fair amount of multifrequency variability data. Hence, the campaign resulted in photometric data in B, V, R, and I bands nearly continuously for 5 days, polarimetric data mainly in R filter for two days, and some near-infrared (NIR) data in J, H, and K filters for a few hours.

To achieve consistency and homogeneity over exposures of multiple observation sites and the instruments, a common set of instructions was followed by the observers. In particular, the same set of comparison stars 3, 4, and 6 from Villata et al. (1998) was used for the photometry. The participating observers carried out photometry for their images using a common set of standard procedures before they provided the data, containing instrumental magnitudes and the uncertainties of the source and the comparison stars in magnitudes, for the final compilation. Table 1 lists the names of the participating observatories along with their locations, telescope sizes, and filters used.

Standard procedures for aperture photometry have been used to extract magnitudes and related uncertainties from the

scientific images after bias, dark, and flat-field corrections. Apertures of about 2–4″, the corresponding number of pixels depending on the instrument and the camera, were chosen so as to have minimum scatter in the comparison stars in the same field. From the data collected by various observers, magnitudes with uncertainties less than 4% were selected for the final compilation. Besides, data exhibiting sudden large jumps from the previous data points were also analyzed carefully before they were included in the analysis. The amount of data that were excluded from the final analysis contribute less than 3% of the total data gathered during the whole campaign. Thus, the numbers of photometric data points included in the final analysis are 548, 776, 1921, and 723 in the filters B, V, R, and I, respectively. The obtained optical light curves in these filters are presented in Figure 1. The accompanying much shorter NIR light curves of S5 0716+71 from the 2014 WEBT campaign in filters J, H, and K are presented in Figure 2.

Unlike the photometric data provided by all the involved observatories, the polarimetric data were mainly obtained with the 70 cm AZT-8 reflector of the Crimean Astrophysical Observatory, the 40 cm LX-200 telescope in St. Petersburg, the 1.8 m Perkins telescope of Lowell Observatory, and the Kanata 1.5 m telescope equipped with HOWPol. The telescopes in Crimea and St. Petersburg use photo-polarimeters based on ST-7 CCDs, whereas Lowell Observatory uses the PRISM camera. For the details on these instruments and the methods the readers are directed to the following references: Larionov et al. (2013) for the AZT-8 reflector and LX-200 telescope, Jorstad et al. (2010) for the Perkins telescope, and Kawabata et al. (2008) for Kanata HOWPol.

3. ANALYSIS AND RESULTS

The gathered photometric data are nearly continuous over the 5-day campaign; however, continuously sampled polarimetric data could be collected only in two 1-day sets separated by a day. Therefore, the analysis is carried out in two parts. The first part includes the analysis of photometric data only, and the
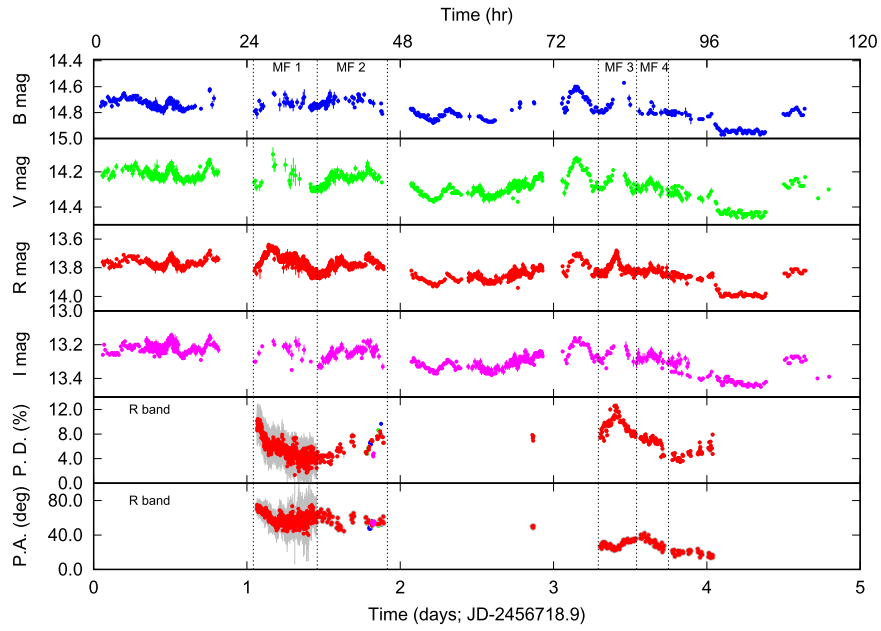
Figure 1. Light curves of S5 0716+714 corresponding to all the data gathered during the 2014 WEBT campaign. In the upper panel, filters *B*, *V*, *R*, and *I* are presented by blue, green, red, and magenta, respectively. In the lower panels, PD (middle) and PA (bottom) in *B* (blue), *V* (green), *R* (red), and *I* (magenta) filters are shown. The dotted vertical lines mark the four microflares with polarimetric coverage analyzed in more detail in Section 3.2.2, and they are labeled here as MF1, MF2, MF3, and MF4.
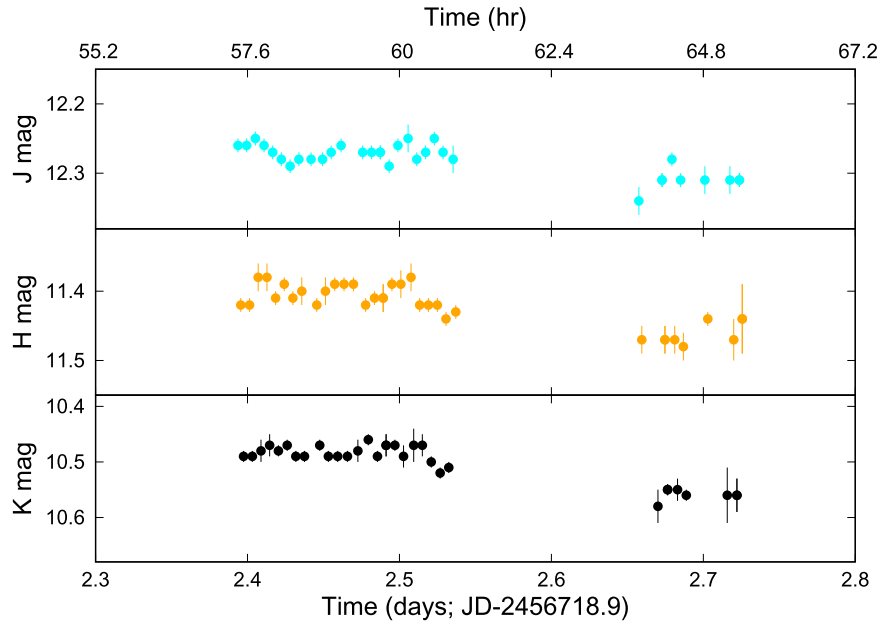
Figure 2. NIR light curves of S5 0716+714 from the 2014 WEBT campaign in filters *J* (cyan; top panel), *H* (yellow; middle panel), and *K* (black; bottom panel).

second part consists of the analysis of the data involving all the photometric and polarimetric data available. The analysis focusing on characteristic variability timescales and correlations between different fluxes in photo-polarimetric bands is presented in the following sections.

3.1. Photometric Data Analysis

The full-campaign mean-normalized light curves in *BVRI* filters are presented in Figure 3. The source brightness in magnitudes was converted into the flux in mJy units by using the zero points for *UBVRI–JHK* Cousins–Glass–Johnsons system given in Table A2 of Bessell et al. (1998), and to

calculate the optical spectra, the fluxes were interstellar extinction corrected using the extinction magnitudes for various filters listed in the NED.[31] As shown in the figure, the photometric data spanned about 112 hr from the start of the campaign, with some interruptions at six locations in time resulting from bad weather conditions and/or a change in active observatories. The corresponding six interruptions were 5.64, 4.33, 1.13, 3.12, and 2.96 hr long, making the net observation exposure 92.83 hr. For about 6 hr, during 99.03–105.22 hr, the source suddenly exhibited a strongly
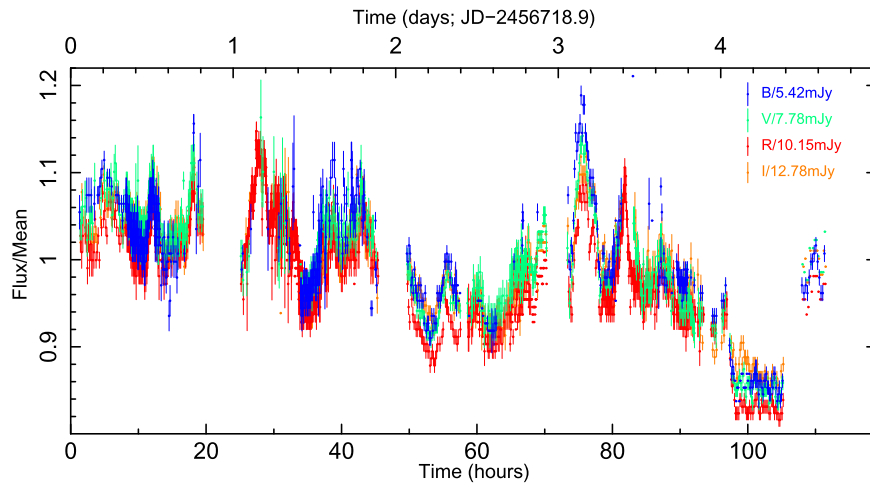
---

[31] https://ned.ipac.caltech.edu/

Figure 3. Mean-normalized photometric light curves of S5 0716+714 in *BVRI* filters (see the upper panels in Figure 1) facilitating a visual comparison of variability across the four bands.

Table 2
Variability Amplitudes of S5 0716+714 during the 2014 WEBT Campaign

Photometric Data			
Filter	Number of Obs.	Mean Mag.	VA (mag)	F_{var} (%)
B	561	14.78	0.38	6.54 ± 0.07
V	776	14.26	0.35	5.74 ± 0.06
R	1921	13.79	0.36	5.79 ± 0.03
I	723	13.28	0.28	5.28 ± 0.05

Polarimetric Data: Epoch I (25–49 hr)		
Obs.	Range	F_{var} (%)
Flux (mag)	13.64–13.86	4.34 ± 0.07
PD (%)	1.32–10.45	25.70 ± 1.00
PA (deg.)	40.15–75.02	10.06 ± 0.55

Polarimetric Data: Epoch II (79–97 hr)		
Obs.	Range	F_{var} (%)
Flux (mag)	13.66–13.88	3.90 ± 0.05
PD (%)	3.45–12.36	27.90 ± 0.30
PA (deg.)	13.59–42.25	22.58 ± 0.37

reduced level of flux variability, resulting in a "plateau" in all four bands' light curves, as seen in Figure 3. The resulting variability duty cycle, excluding this "plateau" period, is thus ~93%. A detailed discussion on this reduced activity will be presented in Section 3.1.4.

Of the four filters analyzed, the data in the *B* filter have the largest scatter and the least number of data points, whereas the data in filter *R* have the least scatter and the largest number of data points. The amplitude of the peak-to-peak variations was estimated by using the relation given in Heidt & Wagner (1996),

$$VA = \sqrt{(A_{max} - A_{min})^2 - 2\sigma^2}, \qquad (1)$$

where A_{max}, A_{min}, and σ are the maximum, minimum, and standard deviation of the light curve, respectively. However, the estimation of this amplitude considers only the two extreme flux measurements and hence may not represent the overall variability during the campaign. Fractional variability F_{var}, on the other hand, includes all the observations and hence provides a better index for the overall variability of the source (see

Edelson et al. 2002; Vaughan et al. 2003). Both of these parameters are listed in Table 2 for *BVRI* filters.

3.1.1. Characteristic Variability Timescales

Study of characteristic variability timescales of blazar light curves proves to be one of the most important tools that can be used to constrain sizes and geometrical structures of blazar emission zones. Small-amplitude flux changes with typical durations of about a few hours are very likely to originate in the closest vicinities of supermassive black holes (SMBHs) launching the jets, and as such may be shaped by a combination of accretion disk instabilities, MHD waves propagating within the outflow, and/or particle acceleration and radiative cooling timescales at the jet base, etc. (see, e.g., Ulrich et al. 1997). A proper characterization of such timescales, along with the search for quasi-periodic oscillations (QPOs), was in fact one of the key motivations to conduct the 2014 WEBT campaign targeting S5 0716+714.

We carried out frequency-domain analysis of the source light curves, as prescribed in Lomb (1976) and Scargle (1982), and
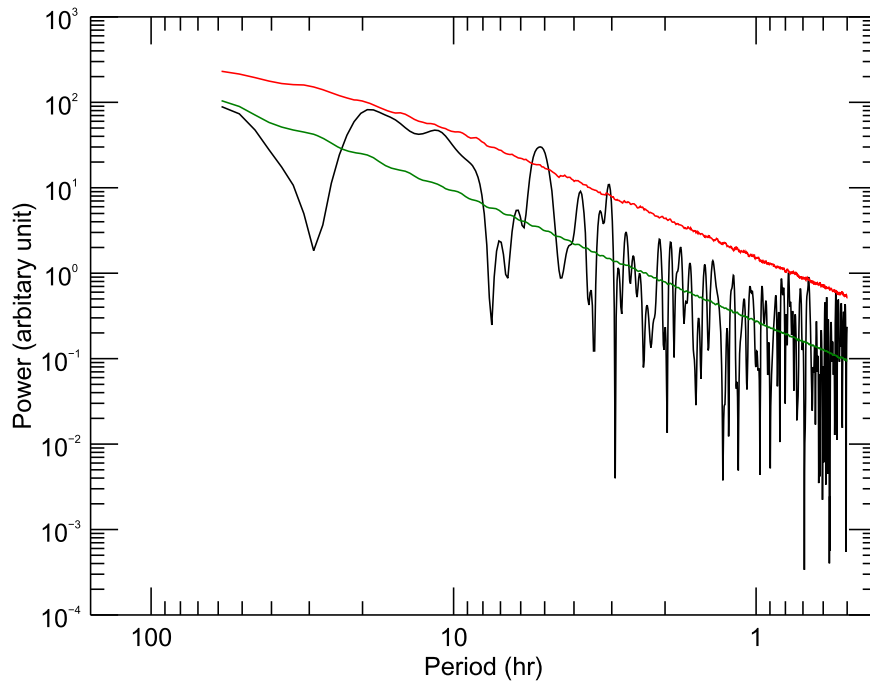
Figure 4. LS periodogram of S5 0716+714 (for the duration of the 2014 WEBT campaign) in *R* filter (black curve), along with the mean periodogram (green curve) and the 99% significance curve (red curve) from the MC simulation.

searched for significant peaks corresponding to possible QPOs. The Lomb–Scargle (LS) periodogram is considered to be a powerful method allowing us to detect and to test the significance of a periodic signal in unevenly sampled and noisy time series. The method, although similar to the ordinary discrete periodogram in many respects, relies on a different approach to spectral analysis, as it estimates the spectral power by the least-squares fitting of the data with a model function of the type $y(t) = A \sin \omega t + B \cos \omega t$. Figure 4 presents the resulting LS periodogram for S5 0716+714 in the best-sampled *R* filter. As revealed by the plot, oscillations with periods of $\simeq 3$ hr and $\simeq 5$ hr *could possibly* be significant enough to indicate the presence of QPOs in the source light curve.

It is important to realize that, however, any analysis of real time series, including the LS periodogram, may be subjected to "spectral leakage" and "aliasing," due to the fact that the analyzed light curve is finite in time, and due to intervals between two successive measurements, in particular in the case of a frequency-dependent (red) noise type of a source variability; similarly, all the monitoring breaks and gaps, unavoidable in any astronomical time series, may distort further the analysis results by introducing spurious peaks in the periodogram (see in this context Press 1978). Therefore, the presence of QPOs in the analyzed light curve should be investigated rigorously. Hence, to estimate the true significance of the peaks present in the LS periodogram, we conducted a significance test using a large number of simulated light curves based on a modeled power spectral density (PSD) function, following the method by Timmer & Koenig (1995). The method relies on randomizing both the phase and amplitude of the Fourier transform coefficients, in order to account for the observed statistical behavior of the periodogram.

First, we estimated the parameters of the PSD, assuming a power-law model that best represents the observed periodogram, according to the power-response method (PSRESP) described in Uttley et al. (2002), which has been widely used in the analyses of AGN variability in general (e.g., Chatterjee et al. 2008; Max-Moerbeck et al. 2014; Chen et al. 2016). Here we briefly summarize the method as follows:

i. For a given time series $f(t_j)$ sampled at times t_j with $j = 1, 2, .., N$, the discrete Fourier power at an angular frequency ω was estimated using the expression

$$P(\nu) = \frac{2\,T}{(N\bar{f})^2} \left| \sum_{j=1}^{N} f(t_i)\, e^{-i2\pi\nu t_j} \right|^2, \qquad (2)$$

where T and $\bar{f}$ represent the total duration of the series and the mean flux of the source, respectively; the periodogram was binned using suitable frequency bins, so as to reduce the scatter in the periodogram for a model fitting.

ii. Based on an arbitrary single power-law model $P(f) = N_0 \times f^{-\beta} + C$ with the added Poisson noise, 1000 source light curves were simulated with the given sampling of the data $f(t_j)$; subsequently, for each simulated light curve binned a discrete Fourier transform (DFT) periodogram was estimated using the same binning as for the data.

iii. For each of the simulated light curves, a χ^2-like quantity (not the same as the conventional χ^2) was calculated using the expression

$$\chi_i^2 = \sum_{\nu_{\min}}^{\nu_{\max}} \frac{[\overline{P_{\text{sim}}(\nu)} - P_i(\nu)]^2}{\Delta\overline{P_{\text{sim}}(\nu)}^2}, \qquad (3)$$

where $\overline{P_{\text{sim}}(\nu)}$ and $\Delta\overline{P_{\text{sim}}(\nu)}$ stand for the mean periodogram and the standard deviation of the 1000 periodograms of the simulated light curves, respectively; a
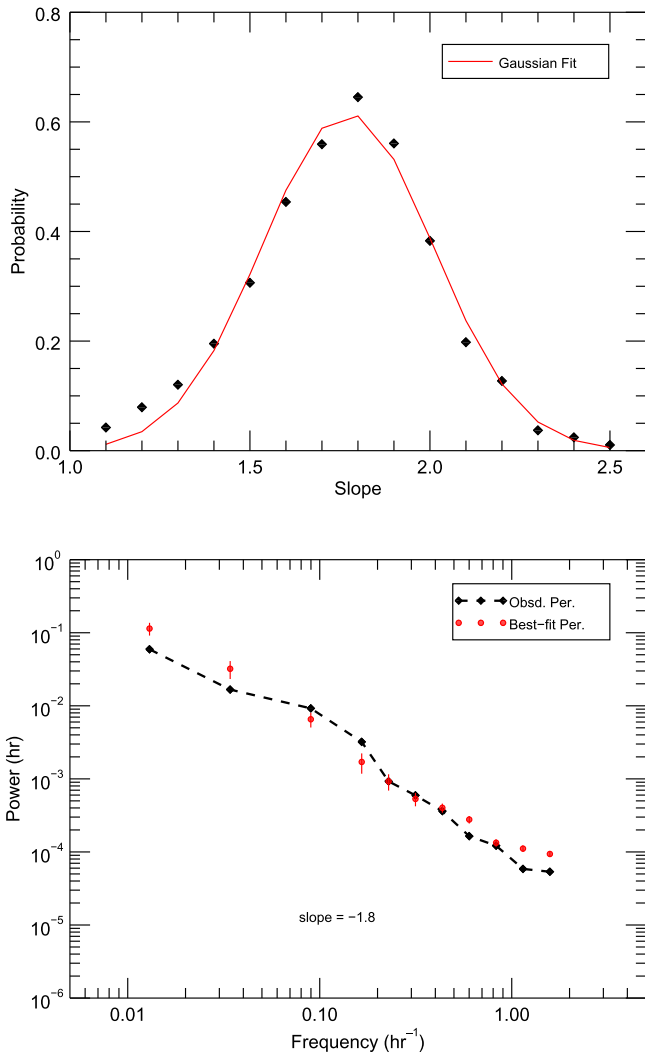
Figure 5. Upper panel: probability distribution of the PSD slopes for S5 0716 +714 (for the duration of the 2014 WEBT campaign) in R filter (black symbols); the red solid line denotes the corresponding Gaussian fit. Lower panel: binned periodogram of S5 0716+71 in R band (black symbols connected by a dotted curve), along with the average of 1000 binned periodograms simulated using the best-fit model slope of $\beta = 1.8$; the errors give standard deviation of the simulated periodograms from the average.

similar quantity for the observed periodogram, χ^2_{obs}, was also evaluated by replacing P_i with P_{obs}.

iv. Step iii was repeated for 15 various slopes of the power-law model.

v. The goodness of fit between the mean simulated periodogram and the observed periodogram was estimated by comparing χ^2_{obs} with χ^2_is; in particular, the ratio of the number of χ^2_is greater than χ^2_{obs} to the total number of χ^2_is in all (15×1000) simulations defined the probability used to quantify the goodness of the fit for a given model. In a situation where the fit statistics is not well understood, such a method involving the use of simulated data for the estimation of goodness of fit is well understood and discussed in Press et al. (1992, Section 15.6).

The resulting probability distribution of the PSD slopes for S5 0716+714 (for the duration of the 2014 WEBT campaign) in R filter is presented in the upper panel of Figure 5. The best-

fit slope (with the highest probability of 0.64) was found to be $\beta = 1.8 \pm 0.3$, where the half-width at half maximum (HWHM) for the Gaussian fit of the slope distribution was associated with the uncertainty in the slope estimate. During the analysis, the slope index, being the primary parameter of interest, was the only parameter varied; the other parameters, N_0 and C, were fixed to $0.97\,h^{-1}$ and $10^{-4}\,h$, respectively. The lower panel in Figure 5 shows the binned mean simulated periodogram, with a slope index of 1.8, and the binned observed periodogram of the source.

Next, with the given best-fit power-law model of the PSD, we simulated 10,000 light curves, which were then resampled to match the sampling of the observed light curve of the source. Subsequently, the distribution of LS periodograms of the simulated light curves was used to estimate the significance of the QPO-like features. The average of the simulated light curves is shown in the upper panel of Figure 4 (green curve), along with the 99% confidence level curve (red curve). The analysis indicates that the power around the periods of 3.05 ± 0.14 hr and 5.17 ± 0.52 hr is significant at the level of 99.68% and 99.91%, respectively. The uncertainties (Gaussian fit HWHMs) associated with the periods of the QPO-like features were estimated by subtracting the simulated mean power level from the observed power.

On the other hand, one should note that the 99% confidence level derived above denotes the "single-trial" confidence bound, i.e., the probability that a periodogram point will exceed this height under the assumption that the null hypothesis model (here: pure red-noise PSD with a power-law slope of 1.8) is correct. We now attempt to estimate the "global" 99% confidence bound, accounting for the fact that we searched over a large number of frequencies. However, the lack of complete independence of neighboring frequencies in the LS periodogram means that the confidence bounds given by Vaughan (2005, Section 4 therein) *cannot* be used at face value, since they were derived for the limit of strictly even sampling.

We find empirically at selected frequencies that the distribution of our LS periodogram points usually follows a rough exponential distribution, but the 99% single-trial confidence bound derived from the simulations indicates a typically $\sim$30% larger dispersion compared to the distribution for the case of even sampling (χ^2_2 distribution, i.e., an exponential probability distribution with variance of 4). Defining z to be the ratio of a periodogram point to the true mean PSD at any given frequency, our simulations indicate that the single-trial 99% confidence bounds typically correspond to values of $z \sim 4$–8. We now make the simplifying assumption that $z = 6$ represents the 99% single-trial probability across all frequencies of interest (compared to $z = 4.6$ for the evenly sampled case). The 99% global confidence bounds can thus be estimated (following Section 3 of Frescura et al. 2008, and paralleling Equation (16) of Vaughan 2005) as $2z \sim -2.6\ln(0.01/n')$, where n' denotes the number of independent frequencies. Using the empirical formula of Horne & Baliunas (1986), we obtain $n' > 1000$, but this value seems overestimated (see Frescura et al. 2008); instead, we take n' to lie in the approximate range 200–800. This range yields a 99% confidence bound of z approximately 12.8–14.7.

The "candidate features" in the LS periodogram at 3 and 5 hr correspond to approximately $z = 8$ and $z = 9$ and the global confidences of approximately 58% and 81%, for $n' = 200$,
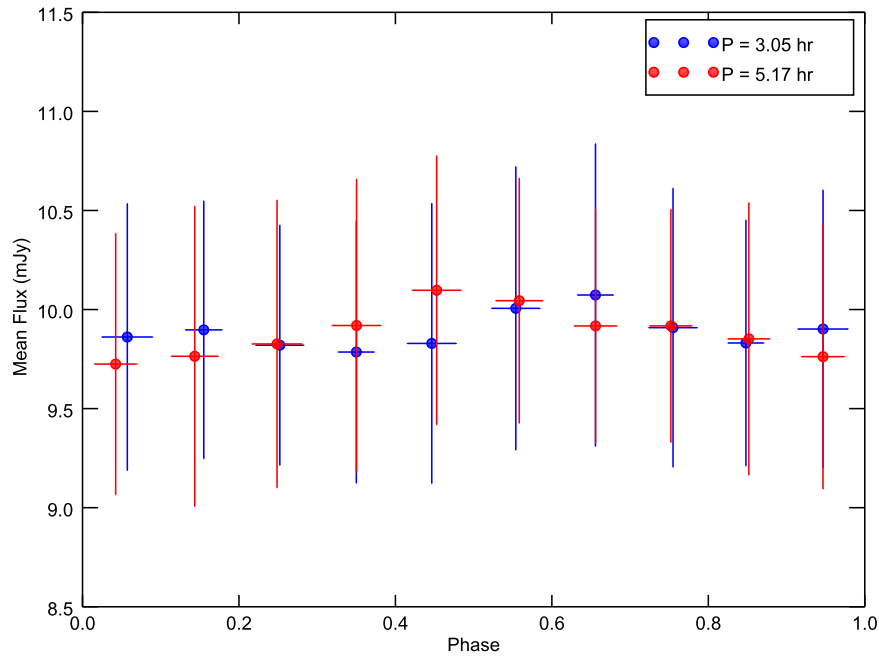
Figure 6. Folded light curve of S5 0716+714 with the periods of 3.05 hr (blue) and 5.17 hr (red).

respectively, so we cannot conclude that these features represent significant deviations from the null hypothesis model. This is supported further by the data folding analysis, the results of which are presented in Figure 6, which does not reveal any significant pulse profiles corresponding to the two periods analyzed. Hence, If there does exist a characteristic timescale, it could simply lie outside the range searched in this paper. Alternatively, the dominant variability processes in S5 0716+714 over timescales of tens of minutes to a few days are scale-invariant.

3.1.2. Correlated Flux Variability

Cross-correlation analysis between different filters offers an important clue about the structure of the blazar emission region and the main radiative processes involved. If the statistical significance of any lag between the flux variation in different bands can be established, such lags could, for example, imply a spatial separation between distinct emission zones dominating radiative output of the source at different frequencies. The discrete correlation function (DCF) discussed in Edelson & Krolik (1988) is one of the most extensively used methods to investigate the cross-correlation between two time series with uneven spacing. In addition, the normalization given in Welsh (1999) was applied to limit the DCF values between −1 and +1 as in the standard correlation function. We calculated the normalized DCF between B and I light curves, which are the bands with the largest wavelength separation in the 2014 WEBT campaign (excluding the JHK ones that span only a few hours). The DCF between B and I light curves and the autocorrelation function (ACF) for the B light curve for a total lag of about half of the total time span of observations are shown in Figure 7. In the figure, the striking resemblance between DCF and ACF suggests that the light curves are highly correlated over the period of time. However, the inlay plot reveals that there could be a marginal lead of the B-band emission over the I-band emission by

$\sim 0.6 \pm 0.11$ hr (the error estimated by HWHM of the Gaussian fit).

3.1.3. Color Variability

During the campaign, the source not only exhibited flux variability but also showed some (relatively moderate) variation in color between B and I bands (~ 1.35 mag), the widest spectral window in the 2014 WEBT data. The apparent correlation between the B flux and the $B−I$ color is shown in the upper panel of Figure 8. The figure is color-coded, so that the observing time runs from blue to yellow. The bottom panel of the figure presents the B-band light curve of the source, for which blue symbols correspond to flat spectra, defined by the lower 30th percentile $B − I$ color value, 1.48, and red symbols to steep spectra, i.e., larger values of $B − I$. As shown, flux maxima appear bluer than flux minima for the analyzed light curve, equivalently to the "bluer-when-brighter" trend claimed for S5 0716+714 already in the past (e.g., Ghisellini et al. 1997; Dai et al. 2013), and found in other BL Lacs as well (e.g., Ikejiri et al. 2011; Wierzcholska et al. 2015, and references therein).

In general, bluer-when-brighter behavior is indicative of a connection between the observed flux enhancement and the episodes of an intensified particle acceleration within the emission site. Changes purely geometrical in nature in the flow beaming pattern, which are expected to lead to rather achromatic flux variability, could not account for the observed trend. Alternatively, spectral flattening witnessed during the elevated flux levels could be explained assuming an underlying steady electron energy spectrum of a curved/concave shape, superimposed on a strongly fluctuating (i.e., occasionally compressed, or amplified) magnetic field; local enhancements in the jet comoving magnetic field intensity B' would then lead to an increased synchrotron emissivity at a given observed frequency, produced by the electrons with correspondingly lower energies $E_e \propto 1/\sqrt{B'}$, and therefore flatter spectrum.
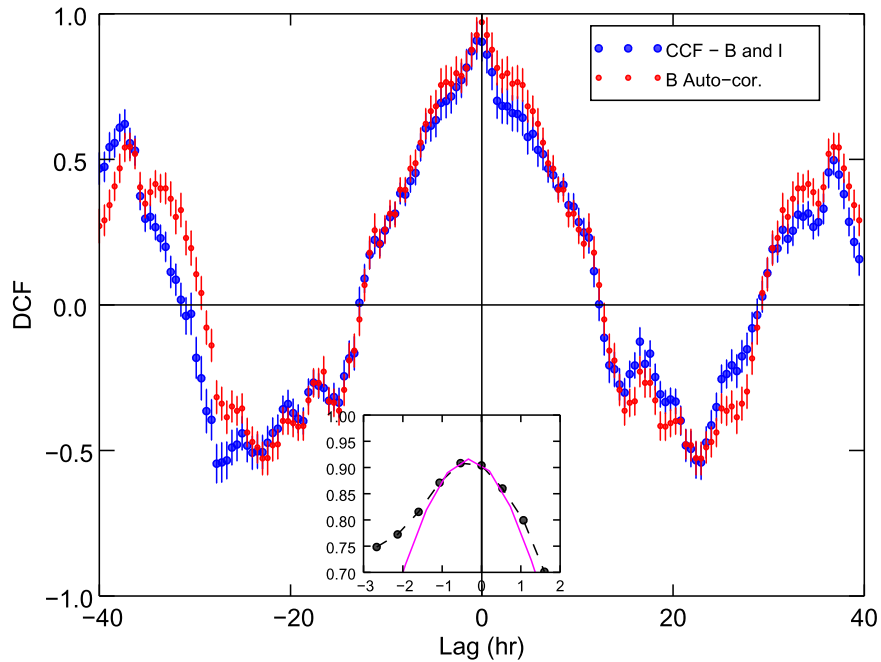
Figure 7. DCF for S5 0716+714 between *B* and *I* fluxes (blue symbols), along with the ACF for the *B*-band flux (red symbols). The inlay plot zooms into the DCF centered around zero lag (black points) and the Gaussian fit (magenta curve). A negative lag here indicates that variations in *B* band lead those in *I* band.

3.1.4. The Plateau

It is interesting to note in Figure 3 that, even though the light curves in all four filters undergo pronounced variations throughout the entire campaign period, as expected in the case of S5 0716+714, famous for its very high flaring duty cycle, at around the 97th hour from the beginning of the 2014 WEBT observation the source suddenly dimmed at all the frequencies by a few tenths of magnitudes and remained at a constant (low) flux level for about 6 hr. In *R* filter, the flux dropped in particular by 0.15 mag down to ∼14.0 mag. Values of F_{var} during the plateau period spanned 1.20%–1.33% ± 0.14%–0.16% across the four bands; locally (over ∼6 hr timescales), F_{var} was typically ∼2%–6% at most other periods in the light curves.

To make sure that this is not an instrumental artifact, we repeated the photometry with the original images several times and checked carefully the data for possible errors. Interestingly, we found a strikingly similar episode of temporary source inactivity in the 2003 WEBT campaign data discussed in Ostorero et al. (2006). The *R* flux at that time fell by about 0.2 mag in about ∼2 hr down to 14.15 mag, and remained constant for about 6 hr. The corresponding segments of the source light curve from both the 2003 (Ostorero et al. 2006) and 2014 (this paper) WEBT campaigns are presented in Figure 9. Surprisingly, no substantial change in the spectral slope was observed during the plateau phase, as shown in Figure 10, indicating that the observed flux during the plateau phase—a power law with spectral index ≳1—is still dominated by the jet, and not, for example, by the accretion disk emission.

3.2. Photo-polarimetric Data: Multivariable Analysis

Apart from the photometric data, the campaign resulted also in the polarimetric data sampled densely in *R* filter (in addition to a few single measurements in *B*, *V*, and *I* filters; see Figure 1). The two well-covered epochs with such polarimetric

data correspond to the time intervals from the 25th to 39th hour and from the 79th to 97th hour from the start of the observation, hereafter referred to as 14 hr long "Epoch I" and 18 hr long "Epoch II," respectively. A detailed study of correlations between the flux, PD, and PA during these epochs is presented in the following subsections.

3.2.1. Correlations between Flux, PD, and PA

In order to investigate the correlation between the observed variations in flux, PD, and PA, we carried out the DCF analysis for the photo-polarimetric data in *R* band collected by the AZT-8, LX-200, Perkins, and Kanata telescopes for both Epoch I and Epoch II. We note that the large error bars that can be seen in the first part of the Kanata polarization data are due to the ongoing maintenance of the reflector of the telescope.

For Epoch I, the calculated DCF between PD and the *R* flux is shown in the upper panel of Figure 11. The analysis reveals a considerably high correlation (DCF value of ∼0.9) with the 2 hr lag, such that the PD variations are leading flux changes. This lag can be seen clearly by eye even in the corresponding normalized light curves (mean subtracted and scaled by standard deviation) presented in the middle panel of the figure. The correlation between PD and PA, on the other hand, was explored through the correlation between Stokes parameters *Q* and *U*. A source evolution on the *Q* − *U* plane, given in the lower panel of the figure, reveals, however, no obvious relation between the PD and PA changes during the analyzed time interval (although note the large error bars).

For Epoch II, on the other hand, a significant correlation with zero lag has been found between the *R*-band flux and PD, implying a certain level of unison between the total and polarized flux changes, as shown in the upper and middle panels of Figures 12. This time, interestingly, PA and PD changes seem more structured as well, as presented in the lower panel of the figure. In particular, for higher fluxes a linear trend between *Q* and *U* can be observed.
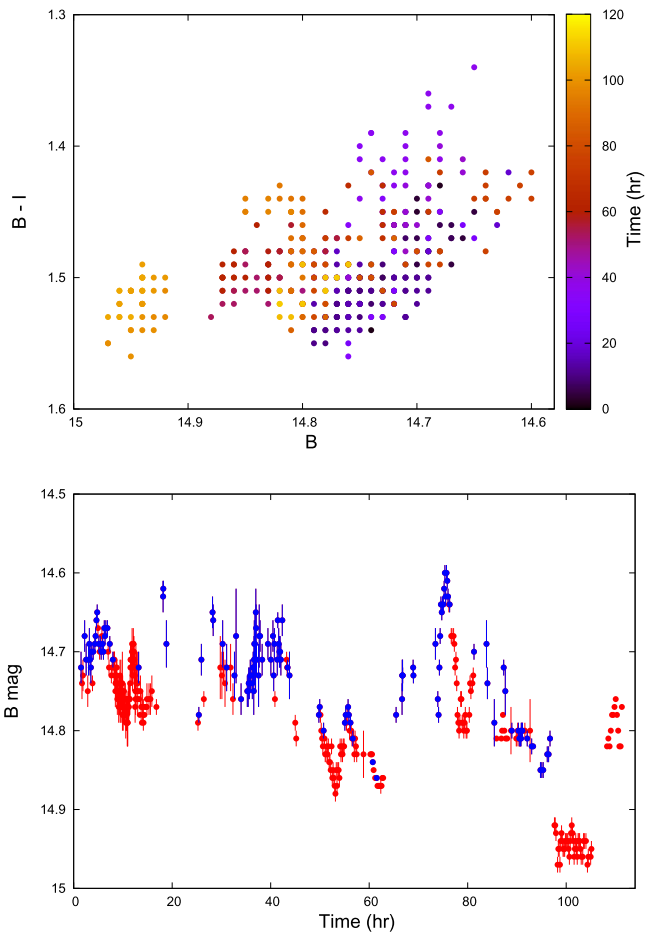
Figure 8. Upper panel: color $B - I$ vs. B magnitude diagram for S5 0716 +714 during the 2014 WEBT campaign; the plot is color-coded so that the observing time runs from blue to yellow; the errors in color and magnitude are not shown for clarity. Lower panel: corresponding B-band light curve of the source, for which blue symbols correspond to flat spectra, defined by the lower 30th percentile $B - I$ color value, 1.48, and red symbols to steep spectra, i.e., larger values of $B - I$.

3.2.2. Modeling of Individual Microflares

As shown in Figures 1 and 3, in addition to a day-long modulation of the S5 0716+714 light curve, we have detected also a number of rapid "microflares" during the 2014 WEBT campaign. Here we attempt to model some of them, assuming that they represent separate and distinct flaring events—"pulse emission" components—superimposed on a relatively slowly varying background component. In particular, making use of the simultaneous flux, PD, and PA measurements, for our analysis we have selected microflares detected during the time intervals 25–34, 34–46, 79–85, and 85–90 hr from the start of the campaign (marked in Figure 1 by dashed vertical lines), which are shown in detail in the first columns of Figures 13–16 (hereafter "microflare 1," "microflare 2," "microflare 3," and "microflare 4," respectively). An in-depth discussion on microflare 3 is presented in Bhatta et al. (2015)

Due to the linearly additive properties of total flux F and the Stokes Q and U intensities, our base assumption regarding the distinctive nature of microflares implies

$$F = F_0 + F_1, \quad Q = Q_0 + Q_1, \text{ and } U = U_0 + U_1, \quad (4)$$

where the "microflare" and the "background" emission components are denoted by indices "1" and "0," respectively. For each analyzed event, background intensities F_0, Q_0, and U_0 are estimated from fitting the data collected just before and just after a given microflare, and next microflaring intensities F_1, Q_1, and U_1 are found, giving us the microflare polarization degree PD_1 and PA χ_1

$$PD_1 = \frac{\sqrt{Q_1^2 + U_1^2}}{F_1} \quad \text{and} \quad \chi_1 = \frac{1}{2}\tan^{-1}\left(\frac{U_1}{Q_1}\right) \quad (5)$$

(for further discussion see Bhatta et al. 2015). The resulting evolutions in intensity and polarization of the selected events are presented in the second and third columns of Figures 13– 16. As shown, all the analyzed microflares are highly polarized, $PD_1 \geqslant 30\%$, but only microflare 3 displays a clear looping behavior in the $Q_1 - U_1$ (or equivalently $PD_1 - F_1$) plane, with
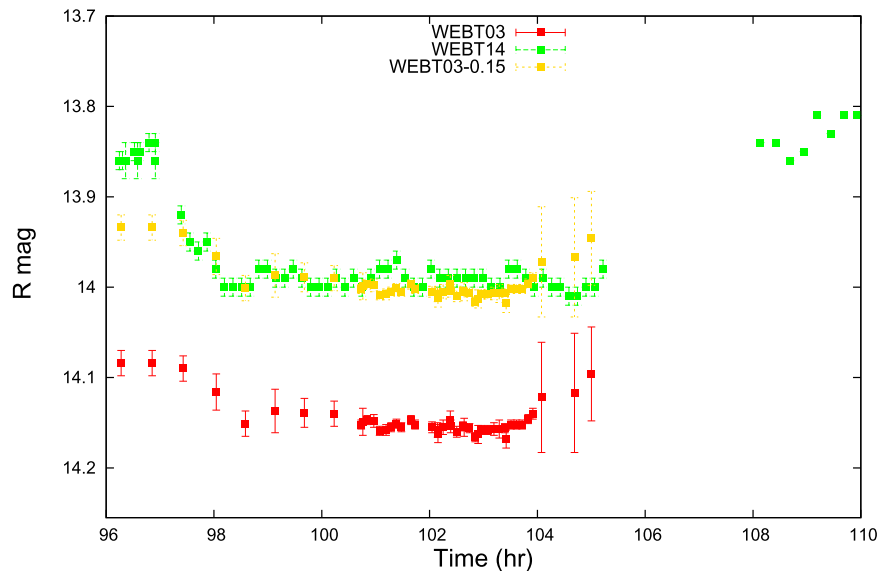

Figure 9. 2014 WEBT light curve of S5 0716+714 in R band during the plateau phase (green symbols), compared with the analogous event detected during the 2003 WEBT campaign (JD 2,452,956.38325–2,452,956.74681; see Ostorero et al. 2006, red symbols), and the same segment of the 2003 light curve just shifted vertically by -0.15 mag (yellow symbols).
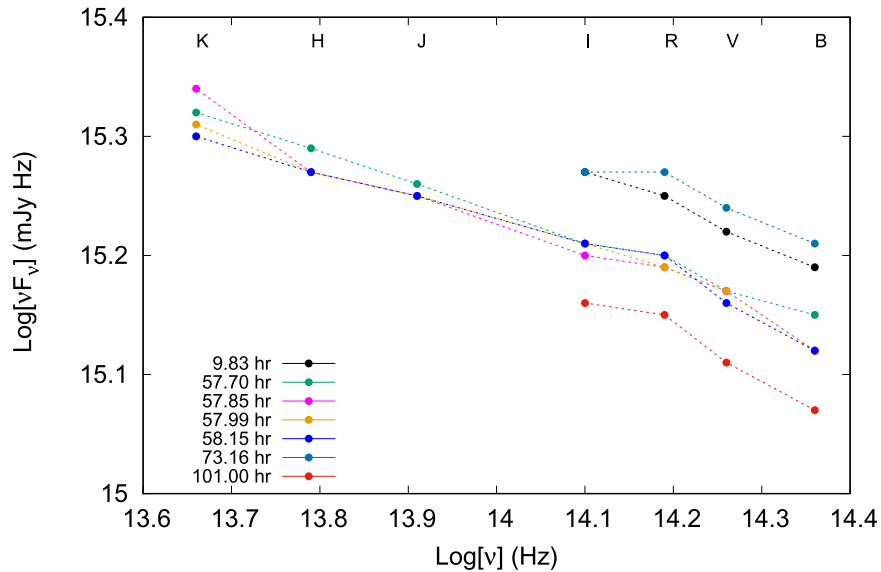
Figure 10. Optical spectra of S5 0716+714 during the 2014 WEBT campaign, at different times of the observations, as indicated in the plot. The letters on the plot represent the filters used. The average spectral slope is $\alpha \simeq 1.2$.

higher PD during the decaying phase of the pulse emission. Microflare 1 exhibits a similar evolutionary pattern, with the overall anticorrelation between the flux and PD, but due to the large observational errors, any clear looping in the $Q_1 - U_1$ plane cannot be identified for this event with high confidence. Hints for the PD/flux anticorrelation can also be seen for microflares 3 and 4.

An interesting difference between Epoch I and Epoch II can be noted here. Namely, while for the first two analyzed microflares 1 and 2 the PA of the pulse emission, $\chi_1 \sim 0°$–$30°$, is larger than that of the background components, $\chi_0 \sim -30°$, being in addition relatively close to the jet position angle ($\sim 45°$ for the innermost parts of the outflow, i.e., within 0.12 mas from the core, and $\sim 20°$ farther down the jet, according to the high-resolution radio image obtained on 2014 February 24 within the VLBA-BU-BLAZAR[32] project; Figure 17), for the latter two microflares 3 and 4 we derive $\chi_1 < \chi_0$ with $\chi_0 \sim 30°$ closely aligned with the jet axis.

4. DISCUSSION AND CONCLUSIONS

The 2014 WEBT campaign targeting S5 0716+714 was organized to monitor the source simultaneously in a number of the optical photo-polarimetric filters, for a longer period of time, in order to investigate in detail the evolution of flux, PD, and PA on timescales ranging from tens of minutes up to several days. The successfully conducted campaign, with participation at many observatories all around the world, resulted in an unprecedented data set spanning ~ 110 hr of nearly continuous, multiband observations (five consecutive days of flux measurements, including two sets of polarimetric data mainly in R filter, lasting each for about 25 hr with no major interruptions). The data were analyzed extensively using different statistical methods and approaches. The main observational findings can be summarized as follows:

1. During the campaign, the source displayed a pronounced variability with peak-to-peak variations of $\gtrsim 30\%$,

consisting of a day-timescale modulation with super-imposed rapid (hourly timescale) microflares character-ized by flux changes by ~ 0.1 mag; in general, variability amplitudes increase with the observing frequency.

2. The overall variability of the source is of the red noise type (consistent with a random-walk process); *some* hints for the presence of QPOs with characteristic timescales of 3 and 5 hr have been found, but the in-depth analysis we have performed regarding these features, including an estimate of a "global" confidence bound in the source periodogram, as well as data folding, reveals that they do not represent highly significant departures from a pure red-noise power spectrum.

3. Flux changes in different bands track each other well, with no significant evidence for any time lags.

4. A "bluer-when-brighter" trend has been found in the source light curve, in the sense that flux maxima appear in general bluer than flux minima, but no tight correlation between the source flux and color could be established.

These results are broadly consistent with what was found before for S5 0716+714, in particular regarding the bluer-when-brighter trend (Ghisellini et al. 1997; Wu et al. 2007; Sasada et al. 2008; Poon et al. 2009; Dai et al. 2013), although we note at the same time that the previous claims regarding the interband variability time lags in the source have often been contradictory (e.g., Villata et al. 2000; Qian et al. 2002; Poon et al. 2009; Wu et al. 2012; Zhang et al. 2012), and also that the previous searches for the source quasi-periodicity were rather inconclusive (Gupta et al. 2008, 2009, 2012).

We argue that the bluer-when-brighter behavior implies that the observed flux enhancements are produced either during the episodes of an intensified particle acceleration or alternatively by the fluctuating magnetic field superimposed on the under-lying steady electron energy distribution with a concave shape. With respect to the source periodocity, we emphasize that the quality of the light curve analyzed here—in particular its duration and uniquely dense sampling—is basically unprece-dented and as such perfectly suited for a search of hour-long QPOs. The fact that we did not find such at a significance level
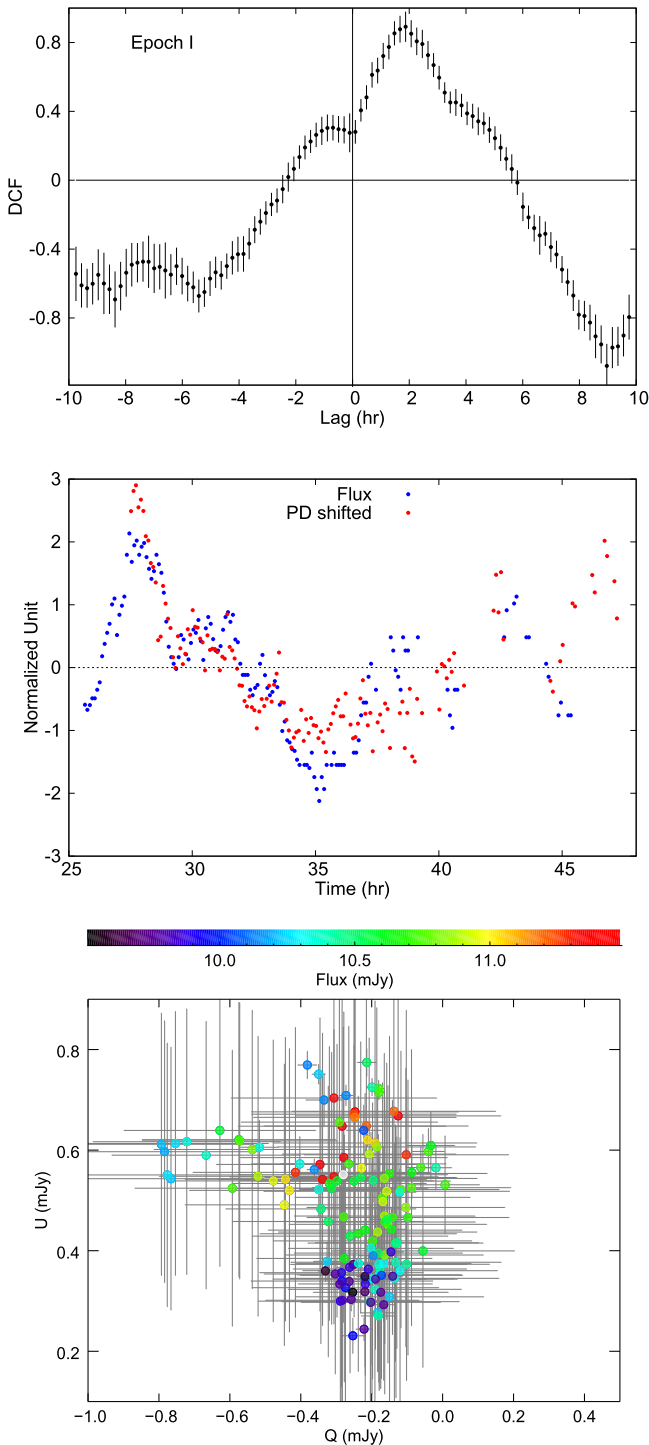
Figure 11. Upper panel: DCF between PD and R flux during Epoch I. A positive lag indicates that PD changes are leading the flux variations. Middle panel: corresponding normalized R-band flux light curve (blue symbols), and the PD light curve shifted horizontally by 1.9 hr (red symbols). Lower panel: corresponding source evolution on the $Q - U$ Stokes parameter plane. The color scale, from purple to red, indicates the corresponding total flux state from low to high.
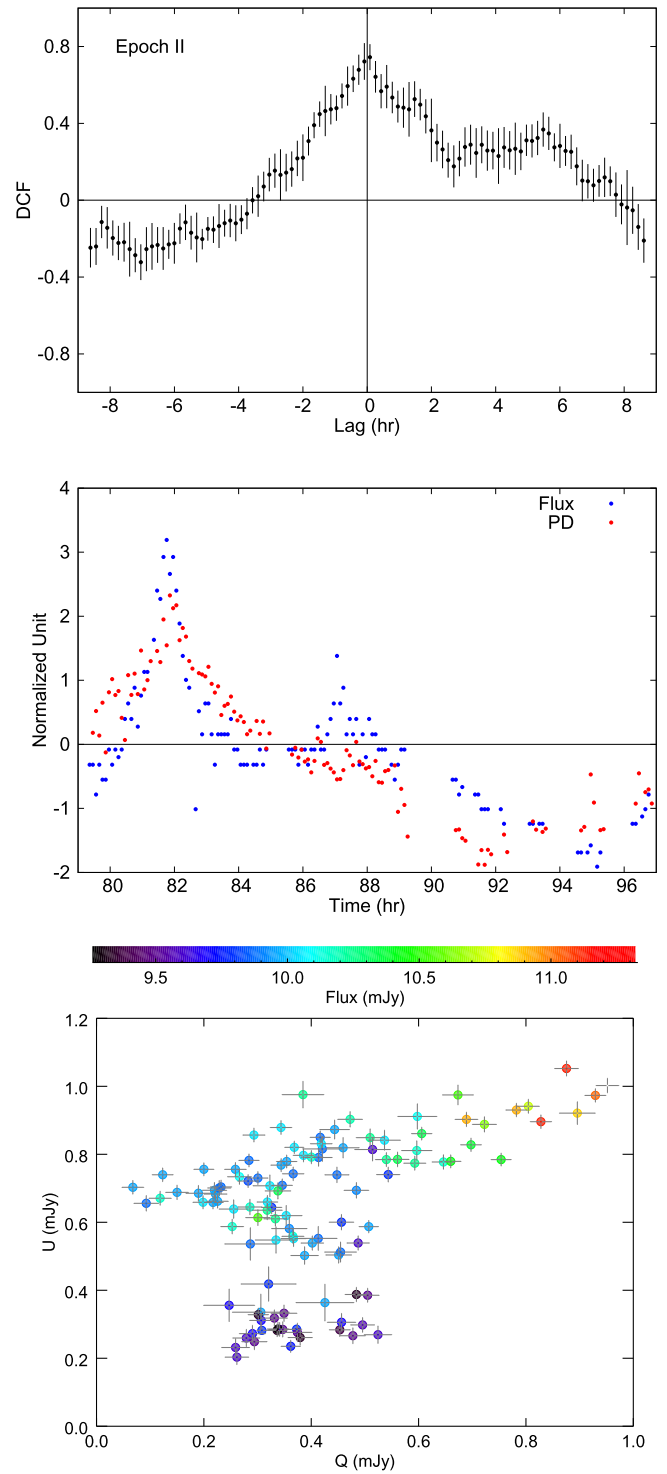
high enough to claim the detection is therefore very meaningful, implying no persistent periodic signal in the source within the analyzed variability timescale domain.

In addition to the above, the 2014 WEBT campaign resulted in very novel, unexpected findings as well, namely:

Figure 12. Same as Figure 11, but for Epoch II.

1. The ∼6 hr long period of the source inactivity has been observed; interestingly, in 2003 the blazar went through a very similar phase, at almost the same "quiescence/plateau" flux level.

2. At a certain configuration of the optical PA relative to the positional angle of the innermost radio jet in the source (Epoch I in Section 3.2), changes in the optical PD led the total flux variability by about 2 hr; meanwhile, at the time when the relative configuration of the polarization and jet
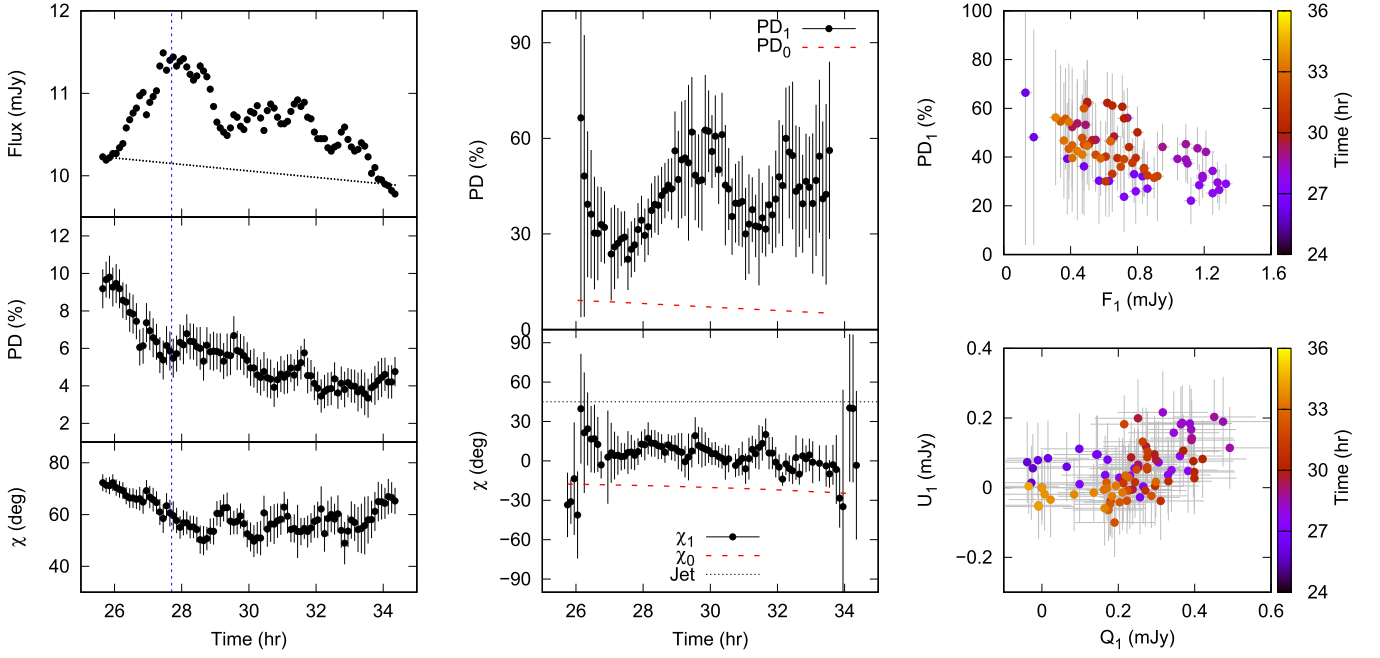
Figure 13. Photo-polarimetric analysis of microflare 1. The panels (from top to bottom) in the first column show the total flux, polarization degree, and polarization angle of the source in *R* band. In the second column, top and bottom panels present the polarization degree and polarization angle of the flaring "pulse" component, respectively, both subtracted from the slowly varying background component indicated in the plots by the dotted curves. The third column shows the variations in the microflare Stokes parameters Q_1 and U_1 (bottom panel), corresponding to the evolution on the $PD_1 - F_1$ plane (top panel). The vertical dotted line on the left column figure marks the segment of the light curve when the PD clearly anticorrelates with the flux.
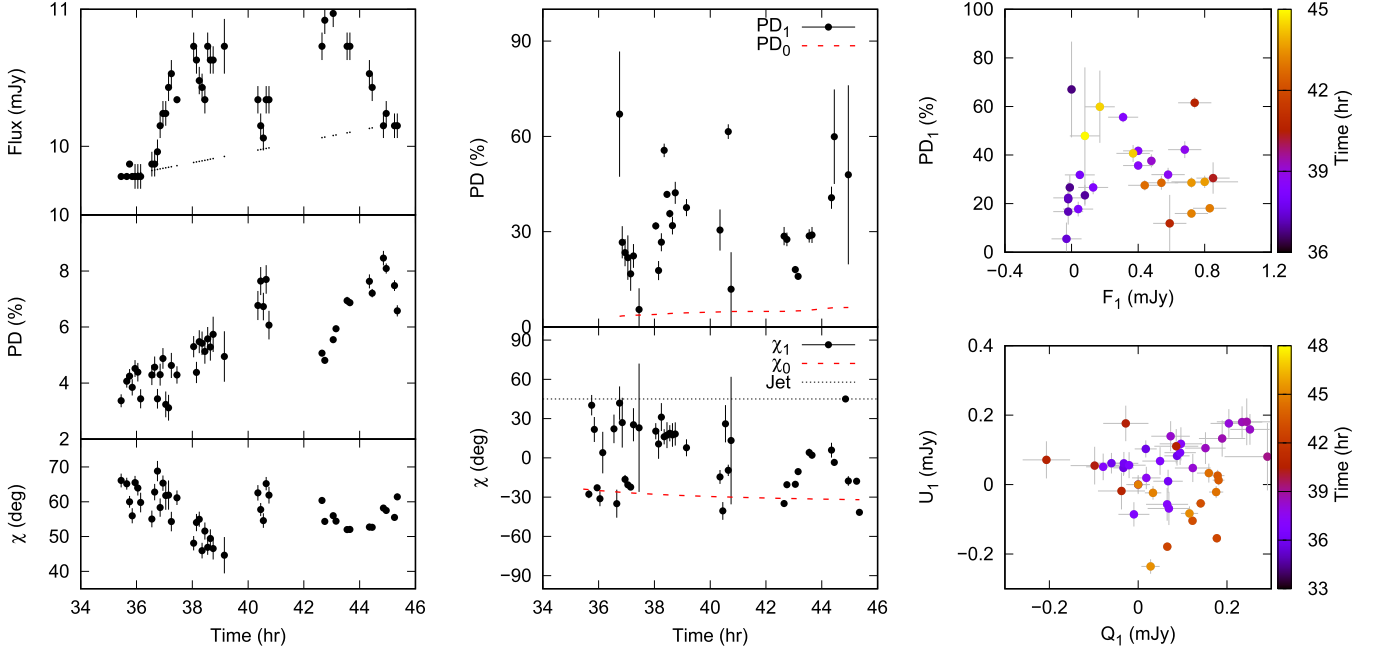
Figure 14. Same as Figure 13, but for microflare 2.

angles altered (Epoch II), no time lag between PD and flux changes could be noted.

3. The microflaring events, when analyzed as separate pulse emission components superimposed over a slowly variable background, are characterized by a very high PD (>30%) and PAs that may differ substantially from the PA of the underlying background component, or from the radio jet positional angle.

The peculiar plateau phase in the source light curve could be explained as resulting from a sudden but only temporary decrease in the jet production efficiency by the central accretion disk/SMBH system. In this scenario, the observed optical emission of the blazar results from a superposition of fluxes produced within some larger portion of the outflow, from subparsec up to parsec scales, such that the emerging flux decreases with the distance, and the characteristic variability
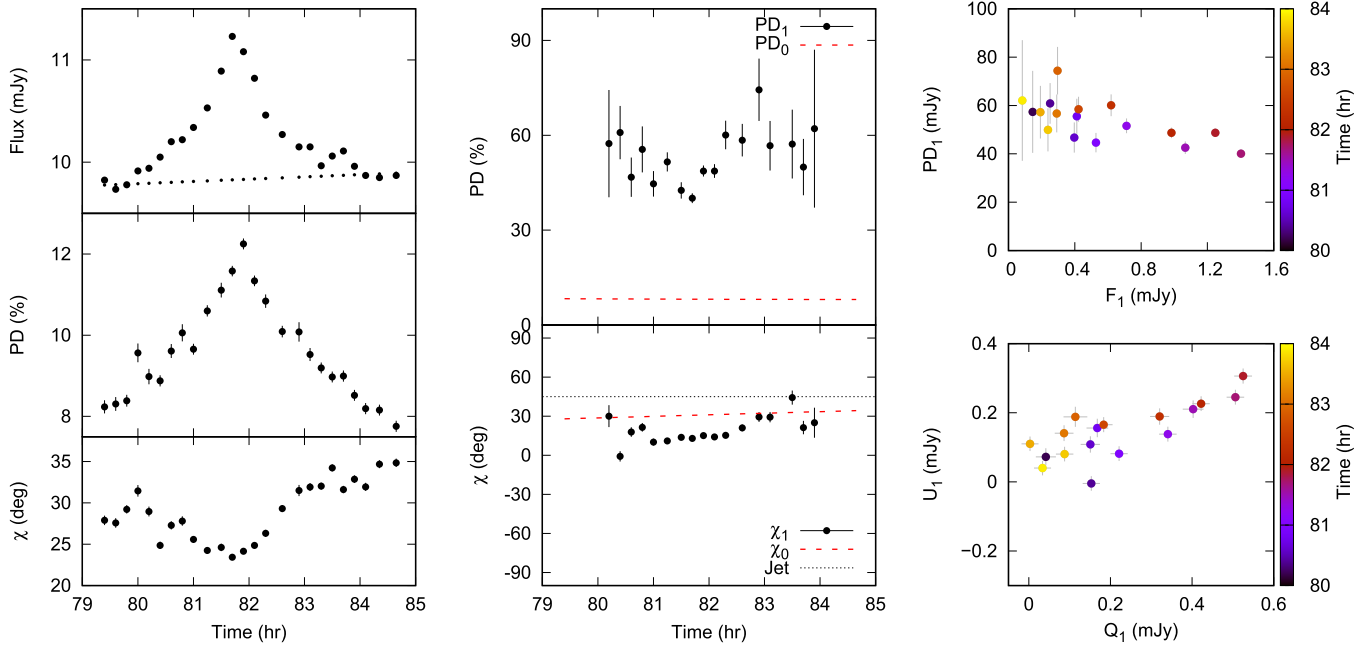
Figure 15. Same as Figure 13, but for microflare 3.
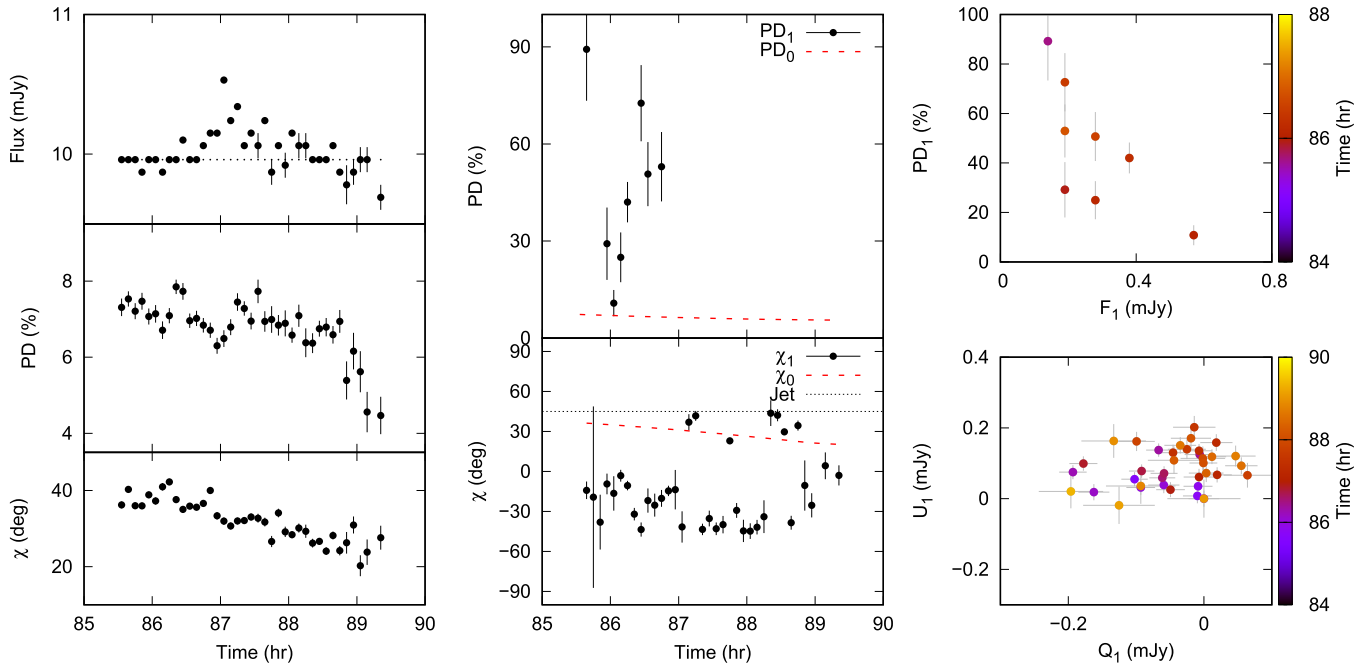

Figure 16. Same as Figure 13, but for microflare 4.

timescale increases (as a result of the jet radial expansion). A sudden disruption of the outflow at the jet base, resulting from some accretion disk instability around the jet launching region, would then result in a short-term "disappearance" of the highly variable innermost emission component, leaving only a slowly variable emission of the outer portions of the jet, and hence manifesting in the source light curve as a distinct plateau.

Note that the optical spectrum during the plateau phase is not much different from that observed during the rest of the 2014 WEBT campaign, indicating that the "plateau flux" is still due to the jet and not the accretion disk emission. Also, the fact that in 2003 a similar plateau has been observed at a similar flux

level, which is, however, *not* a historical flux minimum of the source, indicates that this outer emission component is not completely steady, but instead variable on very long timescales of years and decades.

The 6 hr duration of the observed plateau could be linked to the characteristic timescale for rebuilding the outflow within the jet launching region, for which the *shortest* one would be the Keplerian period around the innermost stable circular orbit (ISCO) of the accretion disk,

$$\tau_K = \tau_g \left(\frac{r_{\rm isco}}{r_g}\right)^{3/2} \simeq 500 \left(\frac{\mathcal{M}}{10^8\,M_\odot}\right)\left(\frac{r_{\rm isco}}{r_g}\right)^{3/2}\,{\rm s}, \quad (6)$$

Clean I map. Array: BHKLMNOPS
0716+714 at 43.135 GHz 2014 Feb 24

Map center: RA: 07 21 53.448, Dec: +71 20 36.363 (2000.0)
Map peak: 1.18 Jy/beam
Contours %: −0.5 0.5 1 2 4 8 16 32 64
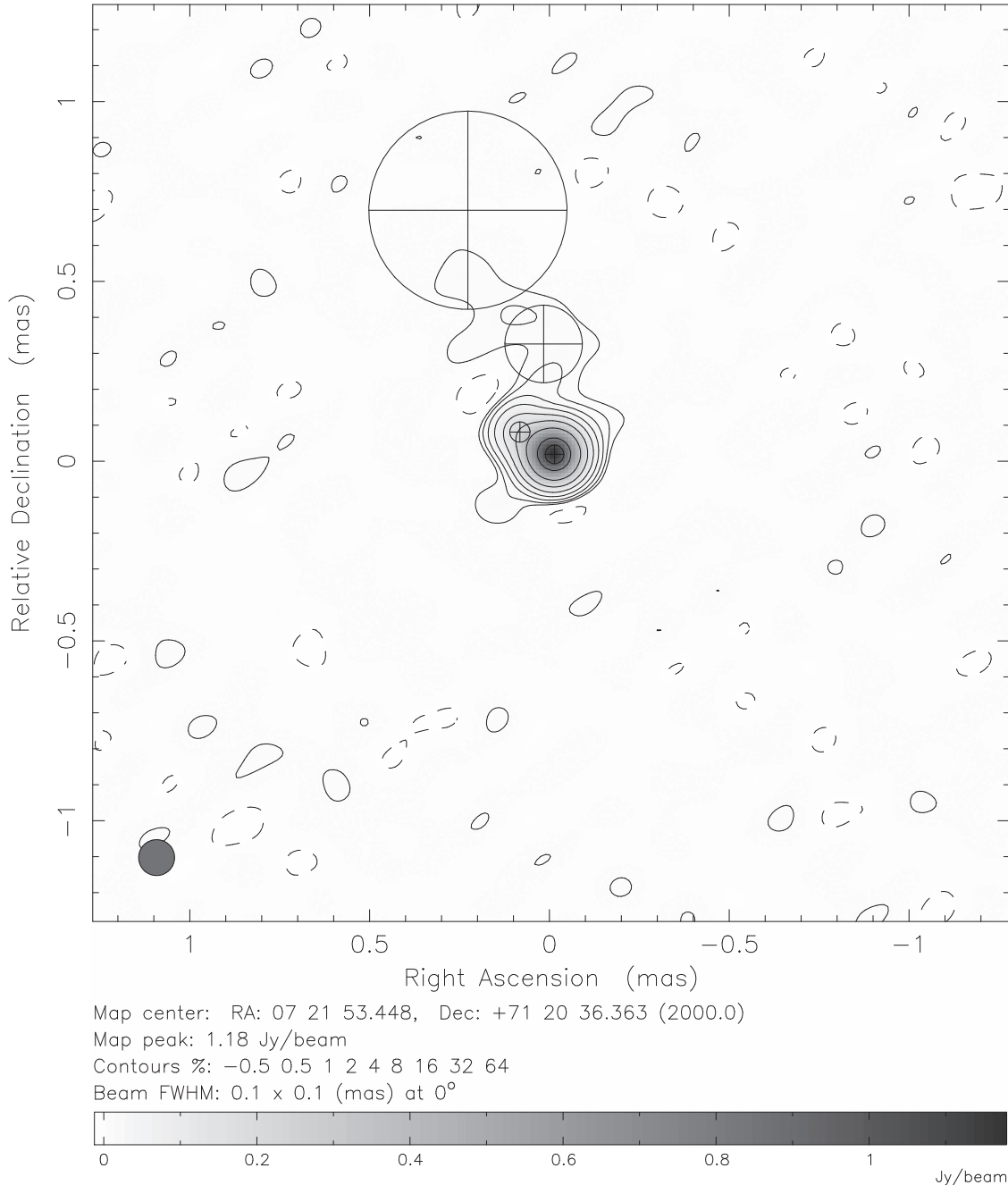Beam FWHM: 0.1 × 0.1 (mas) at 0°

Figure 17. Radio (VLBA-BU-BLAZAR) image of S5 0716+714 obtained at 43.135 GHz on 2014 February.

where $\mathcal{M}$ is the black hole mass and $\tau_g = r_g/c = G\mathcal{M}/c^3$ is the gravitational radius light-crossing timescale (see, e.g., Meier 2012). Hence, the 6 hr interval (seen both in 2014 and also in 2003) would imply $\mathcal{M} \simeq 4 \times 10^9 \, M_\odot$ for the maximally spinning SMBH ($r_{\rm isco} \simeq r_g$), a value that should be considered a safe upper limit for the S5 0716+714 black hole mass, or $\mathcal{M} \simeq 3 \times 10^8 \, M_\odot$ assuming very low spin values ($r_{\rm isco} \simeq 6 \, r_g$).

During the 2014 WEBT campaign, we have also witnessed a very complex relation between the total intensity and the polarization properties of S5 0716+714. In particular, during one brief incidence lasting ∼2 hr, the observed flux was found to be in clear anticorrelation with the PD as marked in the left column of Figure 13 (see also Gaur et al. 2014, for a similar case in the blazar BL Lac in longer timescales), whereas when considering the whole epoch, the changes in the PD were found to be leading the flux changes by about 2 hr. This suggests a delay between the buildup of magnetic flux within the dominant emission region and the onset of an efficient particle acceleration that follows, a behavior that could be reconciled with the scenario in which magnetic reconnection processes play a major role in the jet energy dissipation (see in this context the most recent discussion in Yuan et al. 2016). Yet

during the subsequent epoch the optical PD was well correlated with the optical flux, in agreement with what could be expected from the simplest model of a shock propagating along the jet (see, e.g., Hagen-Thorn et al. 2008, and references therein), so the overall picture may not be unique. Still, the difference between the two epochs involved also a difference in the optical PA, and in particular in an alignment of the PA relative to the jet axis. Hence, it is possible that delays between the magnetic field buildup and the onset of particle acceleration are universal, but can be spotted only in the cases of a particular magnetic field orientation with respect to the jet axis and the line of sight.

A further insight into the energy dissipation processes in S5 0716+714, and other similar blazars, is provided by polarization properties of the shortest timescale and smaller-amplitude fluctuations of the source. Such fluctuations are, in general, believed to be produced within small, possibly independent subvolumes of blazar jets, which could be identified with isolated turbulent cells, magnetic reconnection sites, their mini-outflows, or small-scale shocks induced by such within the main jet body (see in this context, e.g., Narayan & Piran 2012; Bhatta et al. 2013; Marscher 2014; Calafut & Wiita 2015; Chen et al. 2016). Here we have shown that, when modeled as distinct pulses superimposed on a slowly varying background component (see in this context also Hagen-Thorn et al. 2008; Sasada et al. 2008; Sakimoto et al. 2013; Morozova et al. 2014; Bhatta et al. 2015; Covino et al. 2015), such microflares are always highly polarized, but at the same time are characterized by very different PAs that may deviate substantially from the PAs of the underlying background emission.

In Bhatta et al. (2015) we noted that, if blazar microflares are due to small-scale but strong shock waves propagating within the outflow, and compressing efficiently a disordered small-scale jet magnetic field component, one may expect various microflares to be characterized by very different PDs, due to the fact that the expected value of the PD depends strongly on the combination of the shock bulk Lorentz factor and the angle between the shock normal and the line of sight: even small changes in both parameters may result in significant changes in PD! Yet what we observe during the entire 2014 WEBT campaign is that despite vastly different PAs of the microflaring events, the degree of the polarization is always very high. This finding calls for an alternative interpretation of blazar microflares.

REFERENCES

Abdo, A. A., Ackermann, M., Ajello, M., et al. 2010, Natur, 463, 919
Ackermann, M., Ajello, M., Allafort, A., et al. 2011, ApJ, 743, 171
Agarwal, A., Gupta, A. C., Bachev, R., et al. 2016, MNRAS, 455, 680
Agudo, I., Marscher, A. P., Jorstad, S. G., et al. 2011, ApJL, 735, L10
Anderhub, H., Antonelli, L. A., Antoranz, P., et al. 2009, ApJL, 704, L129
Bach, U., Krichbaum, T. P., Ros, E., et al. 2005, A&A, 433, 815
Bessell, M. S., Castelli, F., & Plez, B. 1998, A&A, 333, 231
Bhatta, G., Goyal, A., Ostrowski, M., et al. 2015, ApJL, 809, L27
Bhatta, G., Webb, J. R., Hollingsworth, H., et al. 2013, A&A, 558, A92
Blinov, D., Pavlidou, V., Papadakis, I., et al. 2015, MNRAS, 453, 1669
Calafut, V., & Wiita, P. J. 2015, JApA, 36, 255
Carini, M. T., Walters, R., & Hopper, L. 2011, AJ, 141, 49
Cellone, S. A., Romero, G. E., Combi, J. A., & Marti, J. 2007, MNRAS, 381, 60
Chandra, S., Baliyan, K. S., Ganesh, S., & Joshi, U. C. 2011, ApJ, 731, 118
Chandra, S., Zhang, H., Kushwaha, P., et al. 2015, ApJ, 809, 130
Chatterjee, R, Jorstad, S. G., Marscher, A. P., et al. 2008, ApJ, 689, 79C
Chen, X., Pohl, M., Böttcher, M., & Gao, S. 2016, MNRAS, 458, 3260
Covino, S., Baglio, M. C., Foschini, L., et al. 2015, A&A, 578, A68
Dai, Y., Wu, J., Zhu, Z.-H., et al. 2013, ApJS, 204, 22
Danforth, C. W., Nalewajko, K., France, K., et al. 2013, ApJ, 764, 57
Edelson, R., Turner, T. J., Pounds, K., et al. 2002, ApJ, 568, 610
Edelson, R. A., & Krolik, J. H. 1988, ApJ, 333, 646
Ferrero, E., Wagner, S. J., Emmanoulopoulos, D., & Ostorero, L. 2006, A&A, 457, 133
Foschini, L., Tagliaferri, G., Pian, E., et al. 2006, A&A, 455, 871
Frescura, F. A. M., Engelbrecht, C. A., & Frank, B. S. 2008, MNRAS, 388, 1693
Gaur, H., Gupta, A. C., Wiita, P. J., et al. 2014, ApJL, 781, L4
Ghisellini, G., Villata, M., Raiteri, C. M., et al. 1997, A&A, 327, 61
Goyal, A., Gopal-Krishna, Wiita, P. J., et al. 2012, A&A, 544, A37
Gupta, A. C., Cha, S.-M., Lee, S., et al. 2008, AJ, 136, 2359
Gupta, A. C., Krichbaum, T. P., Wiita, P. J., et al. 2012, MNRAS, 425, 1357
Gupta, A. C., Srivastava, A. K., & Wiita, P. J. 2009, ApJ, 690, 216
Hagen-Thorn, V. A. 1980, Ap&SS, 73, 263
Hagen-Thorn, V. A., Larionov, V. M., Jorstad, S. G., et al. 2008, ApJ, 672, 40
Heidt, J., & Wagner, S. J. 1996, A&A, 305, 42
Horne, J. H., & Baliunas, S. L. 1986, ApJ, 302, 757
Hu, S. M., Chen, X., Guo, D. F., Jiang, Y. G., & Li, K. 2014, MNRAS, 443, 2940
Ikejiri, Y., Uemura, M., Sasada, M., et al. 2011, PASJ, 63, 639
Impey, C. D., Bychkov, V., Tapia, S., Gnedin, Y., & Pustilnik, S. 2000, AJ, 119, 1542
Itoh, R., Fukazawa, Y., Tanaka, Y. T., et al. 2013, ApJL, 768, L24
Jorstad, S. G., Marscher, A. P., Larionov, V. M., et al. 2010, ApJ, 715, 362
Jorstad, S. G., Marscher, A. P., Mattox, J. R., et al. 2001, ApJS, 134, 181
Kawabata, K. S., Nagae, O., Chiyonobu, S., et al. 2008, Proc. SPIE, 7014, 70144L
Kuhr, H., Witzel, A., Pauliny-Toth, I. I. K., & Nauber, U. 1981, A&A, 45, 367
Larionov, V. M., et al. 2013, ApJ, 768, 40
Liao, N. H., Bai, J. M., Liu, H. T., et al. 2014, ApJ, 783, 83
Lomb, N. R. 1976, Ap&SS, 39, 447

Marscher, A. P. 2014, ApJ, 780, 87
Marscher, A. P., Jorstad, S. G., D'Arcangelo, F. D., et al. 2008, Natur, 452, 966
Marscher, A. P., Jorstad, S. G., Larionov, V. M., et al. 2010, ApJL, 710, L126
Max-Moerbeck, W., Hovatta, T., Richards, J. L., et al. 2014, MNRAS, 445, 428M
Meier, D. L. 2012, Black Hole Astrophysics: The Engine Paradigm (Berlin: Springer)
Melrose, D. B. 1994, in ASP Conf. Ser. Vol. 54, The Physics of Active Galaxies, ed. G. V. Bicknell, M. A. Dopita, & P. J. Quinn (San Francisco, CA: ASP), 91
Montagni, F. 2006, A&A, 451, 435
Moore, R. L., Angel, J. R. P., Duerr, R., et al. 1982, ApJ, 260, 415
Morozova, D. A., Larionov, V. M., Troitsky, I. S., et al. 2014, AJ, 148, 42
Narayan, R., & Piran, T. 2012, MNRAS, 420, 604
Nesci, R., Massaro, E., & Montagni, F. 2002, PASA, 19, 143
Nesci, R., Massaro, E., Rossi, C., et al. 2005, AJ, 130, 1466
Nilsson, K., Pursimo, T., Sillanpää, A., et al. 2008, A&A, 487, L29
Ostorero, L., Wagner, S. J., Gracia, J., et al. 2006, A&A, 451, 797
Pollock, J. T., Webb, J. R., & Azarnia, G. 2007, AJ, 133, 487
Poon, H., Fan, J. H., & Fu, J. N. 2009, ApJS, 185, 511
Press, W. H. 1978, ComAp, 7, 103
Press, W. H., Teukolsky, S. A., Vetterling, W. T., & Flannery, B. P. 1992, Numerical Recipes (2nd ed.; Cambridge: Cambridge Univ. Press)
Qian, B., Tao, J., & Fan, J. 2002, ApJ, 123, 678
Raiteri, C. M., Villata, M., D'Ammando, F., et al. 2013, MNRAS, 436, 1530
Raiteri, C. M., Villata, M., Tosti, G., et al. 2003, A&A, 402, 151
Rani, B., Krichbaum, T. P., Fuhrmann, L., et al. 2013, A&A, 552, A11
Rani, B., Krichbaum, T. P., Marscher, A. P., et al. 2015, A&A, 578, A123
Sakimoto, K., Uemura, M., Sasada, M., et al. 2013, PASJ, 65, 35
Sasada, M., Uemura, M., Arai, A., et al. 2008, PASJ, 60, L37
Scargle, J. D. 1982, ApJ, 263, 835
Schneider, P., & Weiss, A. 1987, A&A, 171, 49
Sorcia, M., Benítez, E., Hiriart, D., et al. 2013, ApJS, 206, 11
Stalin, C. S., Kawabata, K. S., Uemura, M., et al. 2009, MNRAS, 399, 1357
Timmer, J., & Koenig, M. 1995, A&A, 300, 707
Tommasi, L., Palazzi, E., Pian, E., et al. 2001, A&A, 376, 51
Tosti, G., Fiorucci, M., Luciani, M., et al. 1998, A&A, 339, 41
Ulrich, M.-H., Maraschi, L., & Urry, C. M. 1997, ARA&A, 35, 445
Uttley, P., McHardy, I. M., & Papadakis, I. E. 2002, MNRAS, 332, 231
Vaughan, S. 2005, A&A, 431, 391
Vaughan, S., Edelson, R., Warwick, R. S., & Uttley, P. 2003, MNRAS, 345, 1271
Villata, M., Mattox, J. R., Massaro, E., et al. 2000, A&A, 363, 108
Villata, M., Raiteri, C. M., Lanteri, L., Sobrito, G., & Cavallone, M. 1998, A&AS, 130, 305
Villata, M., Raiteri, C. M., Larionov, V. M., et al. 2008, A&A, 481, L79
Wagner, S. J., & Witzel, A. 1995, ARA&A, 33, 163
Welsh, W. F. 1999, PASP, 111, 1347
Wierzcholska, A., Ostrowski, M., Stawarz, Ł., Wagner, S., & Hauser, M. 2015, A&A, 573, A69
Wu, J., Böttcher, M., Zhou, X., et al. 2012, AJ, 143, 108
Wu, J., Zhou, X., Ma, J., et al. 2007, AJ, 133, 1599
Yuan, Y., Nalewajko, K., Zrake, J., East, W. E., & Blandford, R. D. 2016, arXiv:1604.03179
Zhang, B. K., Dai, B. Z., Wang, L. P., et al. 2012, MNRAS, 421, 3111